第 42 卷 第 6 期
2021 年 6 月

焊 接 学 报
TRANSACTIONS OF THE CHINA WELDING INSTITUTION

Vol. 42(6):13 − 21
June 2021

焊丝对 T2 紫铜/316L 不锈钢 GTAW 接头组织及性能的影响

朱元皓， 吴宝生， 郭柏征， 李鹏， 董红刚

(大连理工大学, 大连, 116024)

摘要: 采用钨极氩弧焊, 分别填充纯铜焊丝和 307Si 焊丝对 T2 紫铜/316L 不锈钢异种金属进行对接焊, 探究焊丝对铜/不锈钢异种金属接头微观组织、力学性能和耐蚀性的影响. 结果表明, 铁-铜液相分离对焊缝组织的形成起主导作用, 但由于过冷度不同, 填充两种焊丝制备焊缝的液相分离程度不同: 铜焊丝制备焊缝中生成了初次液相分离富铁球, 其内部又发生二次液相分离现象, 生成富铜相; 307Si 焊丝制备焊缝中生成了初次液相分离富铜相, 但富铜相并未呈现二次液相分离特征. 两种焊丝制备接头在拉伸试验中均断裂于铜侧热影响区, 抗拉强度均超过铜母材强度的 80%. 拉伸断口分布着韧窝和延伸区, 呈现典型的韧性断裂特征. 腐蚀及电化学试验结果表明, 与 307Si 焊丝制备接头相比, 铜焊丝制备接头的腐蚀深度差更大, 腐蚀电流密度更高, 耐蚀性更差.

创新点: (1) 填充纯铜焊丝和 307Si 焊丝均得到了无缺陷的铜/钢 GTAW 接头.
(2) 利用 Fe-Cu 液相分离理论解释了铜/钢焊缝组织的形成机制.
(3) 分析了组织不均匀性对纯铜焊丝和 307Si 焊丝制备接头耐蚀性的影响.

关键词: 铜/钢异种金属; 钨极氩弧焊; 微观组织; 力学性能; 耐蚀性

中图分类号: TG 401 **文献标识码:** A **doi:** 10.12073/j.hjxb.20210108003

0 序言

出于节约资源的需要和发挥不同材料优势的必要, 异种材料的焊接成为高端制造业关注的重点[1-3]. 铜/钢异质金属焊接可以将铜良好的导电、导热性与不锈钢的高强度和耐蚀性的特点相结合, 有利于更好发挥两种金属的优势, 已经在很多领域得到应用[4-6]. 但在铜/钢熔焊中, 二者热导率、线膨胀系数等物理性质的巨大差异易导致焊接裂纹[7]; 熔池冷却过程中发生铁-铜液相分离, 易造成焊接缺陷[8].

铜/钢的熔焊中, 铁-铜间的冶金反应对焊缝组织的形成起主导作用. 在冷却过程中, 当熔池的过冷度大于临界过冷度时, 原本无限互溶的液相进入混溶间隙, 发生铁-铜液相分离. 液相分离的机理与调幅分解相似[9], 微小的成分波动会导致周围熔体失稳, 使原本无限互溶的液相分离为两个互不相溶的液相[10]. 液相分离形成的少数相在表面张力作用下形成球体[11], 在基体中形成富铁球或富铜球.

Chen 等人[12] 用液相分离理论解释了激光焊焊缝中初次液相分离所形成的富铜球和其内部形成的二次液相分离富铁球. 液相分离会影响接头的力学性能. Cheng 等人[13] 在使用 MIG-TIG 双面电弧焊对铜/钢进行焊接时发现, 在焊接残余应力作用下, 由于富铁球与铜基体的杨氏模量不同, 富铁球可成为裂纹源, 在接头内部形成裂纹. Meng 等人[14] 认为, 均匀分布的液相分离富铁相可以增强铜基焊缝. 熔池中充分的液相分离产生的大量均匀分布富铁球阻碍了铜晶粒的生长, 有利于细小等轴晶的形成.

目前铜/钢熔焊相关研究仅分析了铁-铜液相分离对接头力学性能的影响. 但由液相分离控制的铜/钢焊缝微观组织的形成机理尚未得到深入研究. 另外, 铜/钢复合结构多应用于舰船海水管路和核岛冷却系统中, 但有关铜/钢焊接接头腐蚀行为的研究却很少. 采用钨极氩弧焊 (GTAW), 分别填充纯铜焊

收稿日期: 2021 − 01 − 08

基金项目: 国家自然科学基金资助项目 (51674060)

丝和 307Si 焊丝对 T2 紫铜/316L 不锈钢异质金属进行焊接，分析铁-铜液相分离对两种焊丝制备焊缝组织的影响，并对接头的力学性能和腐蚀行为进行了研究.

1 试验方法

采用 GTAW 对 1 mm 厚 316L 不锈钢和 T2 紫铜进行对接焊，焊丝选用直径为 1.2 mm 的纯铜焊丝和 307Si 焊丝. 母材和焊丝的化学成分见表 1.

表 1 母材和焊丝的化学成分 (质量分数，%)
Table 1 Chemical composition of base materials and filler wires

材料	Ni	Cr	Mo	Mn	Si
316L	10.56	17.50	2.07	1.06	0.43
T2	—	—	—	—	≤ 0.03
Cu焊丝	—	—	—	≤ 0.5	≤ 0.5
307Si焊丝	8.78	19.3	—	6.57	0.86
材料	P	S	Sn	Fe	Cu
316L	≤ 0.03	≤ 0.03	—	余量	0.05
T2	≤ 0.01	≤ 0.01	—	—	余量
Cu焊丝	—	—	≤ 1.0	—	余量
307Si焊丝	0.014	0.004	—	余量	—

焊前用 240 号砂纸去除母材端面上的氧化膜和机加工痕迹，然后用酒精清洗母材以去除油污. 保护气体为氩气，流量为 10 L/min. 焊接工艺参数见表 2.

表 2 焊接工艺参数
Table 2 Welding experiment paraments

焊丝	焊接电流 I/A	送丝速度 v_g/(mm·s^{-1})	行走速度 v_w/(mm·s^{-1})
铜焊丝	130	6	1
307Si焊丝			

2 结果与分析

2.1 宏观形貌

焊缝外观与接头截面的宏观形貌如图 1 所示. 由于焊接时采用了直流反接模式，电弧稳定，焊缝周围无飞溅. 焊接参数选取适当，未造成咬边、表面裂纹等缺陷. 从接头的截面形貌可知，两种焊丝与

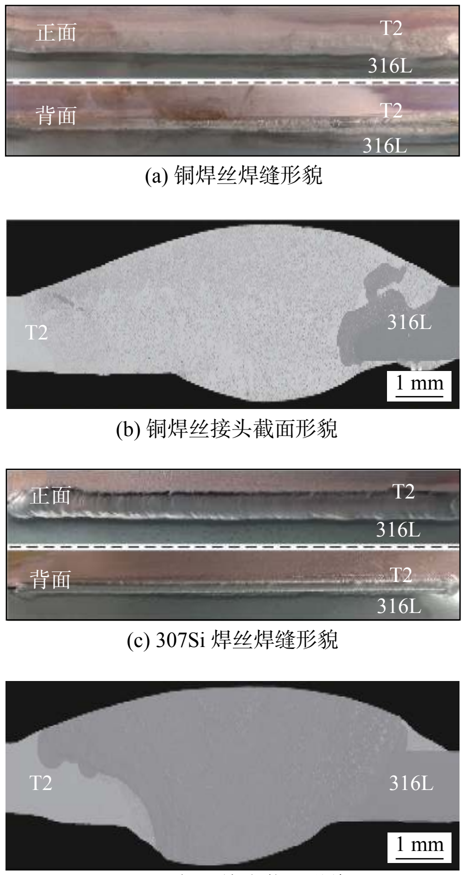

(a) 铜焊丝焊缝形貌
(b) 铜焊丝接头截面形貌
(c) 307Si 焊丝焊缝形貌
(d) 307Si 焊丝接头截面形貌

图 1 两种焊丝制备焊缝的宏观形貌
Fig. 1 Macroscopic morphology of the joints achieved by two filler wire. (a) the joints by copper filler wire; (b) the joints section by copper filler wire; (c) the joints by 307Si filler wire; (d) the joints section by 307Si filler wire

母材间均具有良好的润湿性. 接头内部无铜/钢焊接时常见的气孔、热裂纹、渗透裂纹等缺陷.

2.2 微观组织

2.2.1 纯铜焊丝制备焊缝

当采用纯铜焊丝焊接铜/钢时，焊缝微观组织主要由铁-铜之间的液相分离所控制. 焊缝内的特征组织之一是图 2a 所示的富铁球. 根据 Fe-Cu 二元相图[15] 可知，当熔池的过冷度大于 ΔT_C 时 (ΔT_C 为过冷度阈值，即一定成分下液相线和混溶间隙之间的温差[11])，无限互溶的液相发生初次液相分离，生成富铁液滴，其在随后的冷却过程中形成富铁球；富铁球还可能发生二次液相分离，在基体中形成富 Cu 液滴，在凝固过程中形成富 Cu 析出相.

从图 2b 中球内析出相的高倍图像可以看出，富铁球中析出相的组成并不单一. 富铁球的成分分析结果见表 3. 根据 A 点成分和 Fe-Cu 二元相图可知，A 处深灰色相为 Fe 在 ε-Cu 中的过饱和固溶

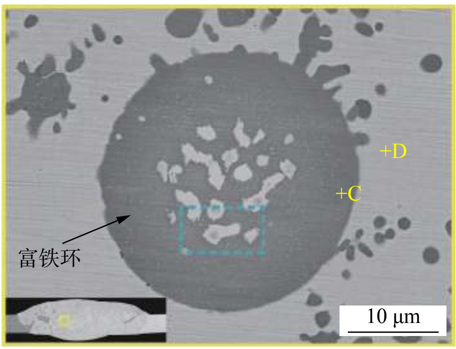

(a) 富铁球

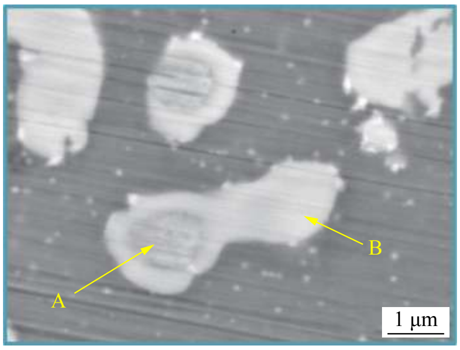

(b) 球内析出相

图 2　铜焊丝制备焊缝特征组织

Fig. 2　Characteristic microstructure of the weld produced by Cu filler wire. (a) Fe-rich spherulite; (b) internal precipitate

体, 标志着 Fe 和 Cu 间二次液相分离的发生. 然而这并不是富铁球中发生的唯一反应. 根据 B 处成分和 Fe-Cr-Mo 三元相图[16] 可以推测 B 处浅灰色相为 Fe-Cr-Mo 间形成的金属间化合物 (IMC)σ 相. 由图 3 析出相元素分布图可知, σ 相主要依附或包裹于二次液相分离形成的富 Cu 球. Gao 等人[17] 也在纯 Mo/不锈钢激光焊中检测到 σ 相, Yang 和 Busby[18] 通过热力学模拟和动力学模拟证实了 316L 不锈钢中存在 σ 相. 虽然 σ 相在平衡状态下的分解温度约为 472 ℃, 但由于焊接过程中的冷却速度很快, 并且 Cr 元素对其起稳定作用, 故 σ 相仍能在室温下存在.

从富铁球的形貌和定量分析结果可知, 其外围存在富铁环. 富铁环的形成与球内析出相的运动有关. 在富铁球内部, 富铜球和 σ 相在表面能差的驱动下发生运动. 由温度差引起的表面能差[19] 使析出相向富铁球中心运动; 由浓度差引起的表面能差[20] 使析出相向富铁球表面运动. 在合力的作用下, 析出相向富铁球中心呈球状聚集, 在富铁球外围形成富铁环.

图 4 展示了富铁球中析出相的各种形态, 反映了球内析出相在凝固过程中的演变行为. 图 4a 为液相分离和析出的初始阶段, 细小的析出相在富铁球内均匀弥散的分布. 随着冷却的进行, 纳米尺寸的析出相在表面能差的作用下向富铁球中心聚集. 在此过程中, 原本均匀分布的纳米颗粒聚集并粗化, 如图 4b, 4c, 最终演变成如图 4d 所示的团块状.

表 3　富铁球 EPMA 定量分析结果

Table 3　EPMA quantitative analysis results of Fe-rich spherulite

位置	元素含量 a(%)					可能相
	Fe	Cu	Cr	Ni	Mo	
A	10.2	80.4	4.2	1.5	3.6	富铁ε-Cu
B	48.7	2.0	26.0	2.4	20.9	σ
C	66.1	5.6	18.9	3.9	5.4	α-(Fe, Cr)
D	2.8	95.1	0.7	1.3	0.0	ε-Cu

焊缝中除富铁球外, 还存在富铁枝晶, 如图 5 所示. 富铁枝晶是铁-铜熔体液-固转变过程中在铜基焊缝中形核, 并在冷却过程中长大的 γ-Fe, 即

$$L \rightarrow \gamma\text{-Fe} + L' \qquad (1)$$

2.2.2　307Si 焊丝制备焊缝

焊缝内的组织及成分定量结果分别如图 6a, 6b 和表 4 所示. 使用 307Si 焊丝焊接不锈钢与铜时, 焊缝中仍会发生铁-铜液相分离. 但与铜焊丝制备焊缝相比, 307Si 焊丝制备焊缝中液相分离富铜相分布比较集中, 且无二次液相分离特征.

焊缝中富铜相的集中分布与 307Si 焊丝制备熔池和铜焊丝制备熔池冷却速度的差异有关. 液态钢的导热率远小于液态铜的导热率, 307Si 焊丝制备熔池的冷却速度较小. 因此熔池中液相冷却速度慢, 难以制造负温度梯度, 产生的过冷度小. 而高熔点成分在冷却过程中率先凝固, 富铁相液-固转变界

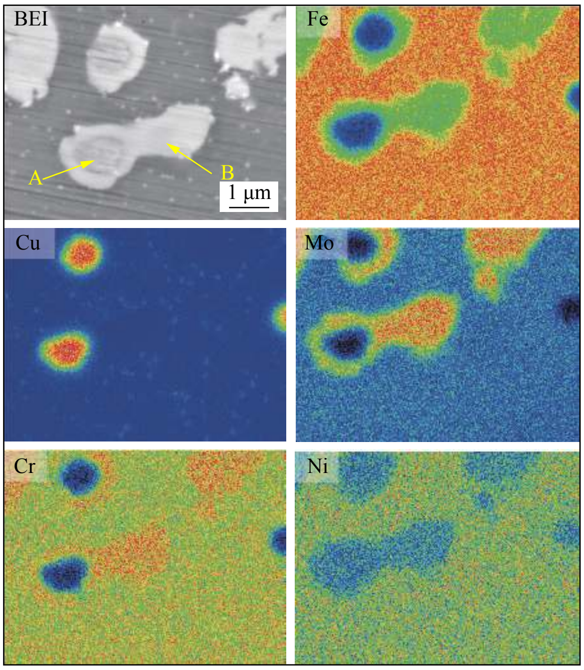

图 3 富铁球内析出相元素分布

Fig. 3 Elemental distribution of precipitate in Fe-rich spherulite

面前沿排出铜原子，在局部形成成分过冷，所以初次液相分离形成的富铜相均在先凝固的组织前沿聚集，利用成分过冷形核；焊缝中剩下的富铜液相在富铁相凝固过程中被排到枝晶间隙，呈现各异的形状.

初次液相分离生成的富铜相并未发生二次液相分离，在内部析出富铁相. 铜为液相分离少数相的情况下，Wu 等人[19] 也未在初次液相分离产生的富铜球中发现二次液相分离现象. 这是由于液相分离所形成富铜相液滴的过冷度比富铁相液滴的过冷度小，不足以发生二次液相分离. 从富铜相的成分也可以发现，其铁含量远高于室温下铁-铜间的极限溶解度，这表明富铜相凝固过程中发生了显著的溶质截留. 这也印证了富铜相未能发生液相分离将过饱和的铁释放.

焊缝中除了初次分离富铜相外，还分布着许多深色相，如图 6b 中的 C 点所示. 由定量分析结果和铁-铬二元相图可知，这些深色相为 α-(Fe, Cr) 固溶体. 深色相均由一层铜膜包裹，这是因为初次液相分离生成的富铜液相与已凝固的富铁相中的铁发生包晶反应，即

$$L(Cu) + \gamma\text{-Fe} \rightarrow \varepsilon - Cu \tag{2}$$

反应并不完全，从而生成了一层铜膜包裹住剩余反应物.

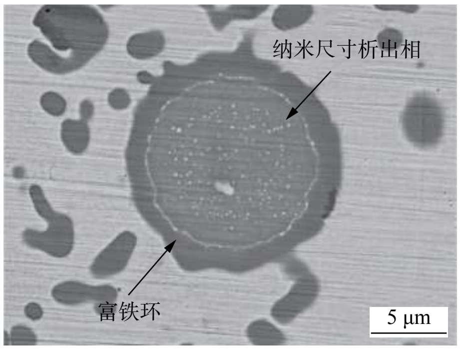

(a) 纳米尺寸析出相

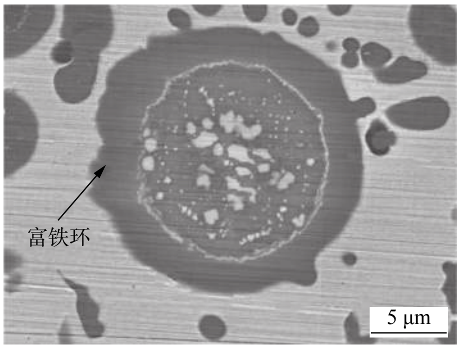

(b) 纳米尺寸析出相和团块状析出相

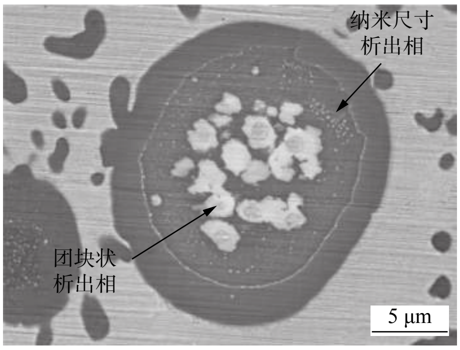

(c) 纳米尺寸析出相和粗化团块状析出相

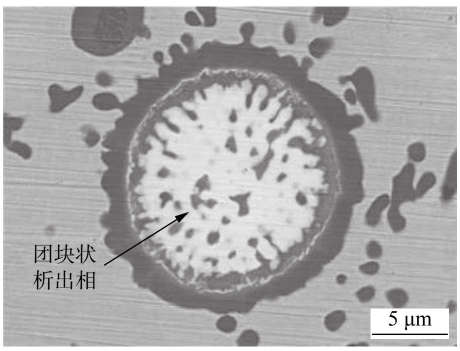

(d) 团块状析出相

图 4 富铁球内不同形态的析出相

Fig. 4 Various shapes of precipitates in Fe-rich spherulites. (a) nano-sized precipitates; (b) nano-sized and bulky precipitates; (c) nano-sized and coarsened bulky precipitates; (d) bulky precipitates

在钢侧界面附近的熔合区中也存在深色相，熔合区形貌和定量分析结果分别如图 6c, 6d 和表 4

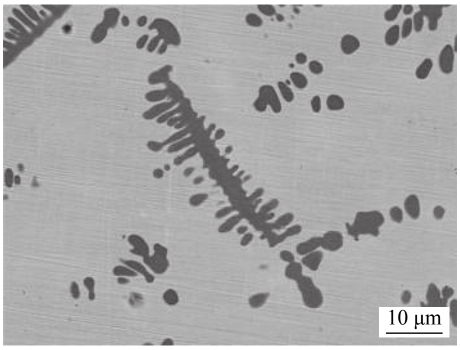

图 5　铜焊丝制备焊缝中的富铁枝晶

Fig. 5　Fe-rich dendrites in copper-based weld produced by copper filler wire

所示. 其成分和形成机理与焊缝中的深色相有所不同. 熔合区中深色相形成的本质是晶体结构变化. 处于熔合区的钢母材在焊接过程中被加热到液相线以上，而 316L 不锈钢的凝固类型为奥氏体-铁素体型，因此不锈钢在冷却过程中部分发生相变，由奥氏体转变为铁素体. 由铁-铬相图可知，铬元素是铁素体形成元素，在体心立方 (BCC) 相中的溶解度比在面心立方 (FCC) 相中大，在 FCC 相中溶解度不足 20%. 故相变过程中铬元素向铁素体相中迁移，导致 BCC相铬含量升高，在背散射电子图像中呈现深色.

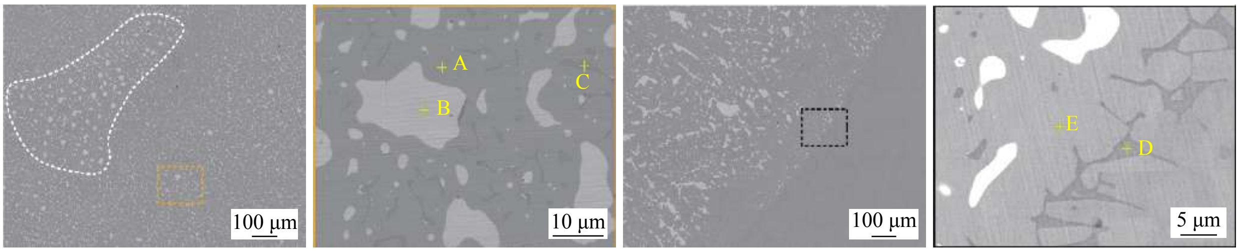

(a) 焊缝　(b) 图 6a 中区域放大　(c) 钢侧界面　(d) 图 6c 中区域放大

图 6　307Si 焊丝制备接头组织形貌

Fig. 6　Morphology of joint produced by 307Si filler wire. (a) weld zone; (b) high-magnification image of orange box in Fig. 6a; (c) weld/316L interface; (d) high-magnification image of black box in Fig. 6c

表 4　307Si 焊丝制备的焊缝中 EPMA 定量分析结果

Table 4　EPMA quantitative analysis results in weld zone produced by 307Si filler wire

位置	元素含量 a(%)						可能相
	Fe	Cu	Cr	Ni	Mn	Si	
A	63.6	7.7	17.2	7.3	2.7	1.3	γ-Fe
B	9.2	79.5	3.5	4.5	2.9	0.2	ε-Cu
C	64.5	2.9	25.7	3.1	2.3	1.0	α-(Fe, Cr)
D	67.5	2.5	23.0	4.6	1.3	1.1	α-Fe
E	67.3	5.6	16.9	6.6	2.5	1.1	γ-Fe

2.3　拉伸性能

拉伸试验结果如图 7 所示. 在铜焊丝制备接头的拉伸试验中，铜侧热影响区为力学性能的薄弱区域，拉伸试样均断裂于此. 接头平均抗拉强度为 219.6 MPa，达到铜母材 (268.0 MPa) 的 81.7%. 在拉伸试验过程中，由于富铁相与铜基体的模量不同，可能出现应变错配. 但铜基体具有良好的塑性，能有效地弥合应变错配，因此在拉伸试验中富铁相并未发展成裂纹源.

307Si 焊丝制备的拉伸试样同样断裂于铜侧热影响区，因此抗拉强度与铜焊丝制备接头接近，为

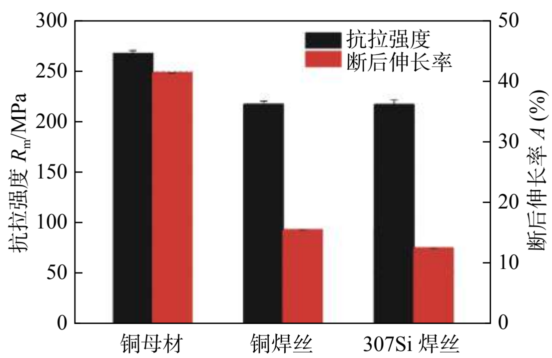

图 7　拉伸试验结果

Fig. 7　Result of tensile test

217.1 MPa.

铜焊丝制备接头的拉伸断口形貌如图 8a, 8b 所示. 断口的局部区域存在韧窝, 韧窝的底部分布着第二相颗粒, 它们导致了微孔洞的形成. 虽然韧窝的分布并不广泛, 但断口上存在着韧性断裂的另一个重要特征—延伸区[21], 如图 8b 所示. 当塑性变形发生时, 位错沿多个滑移系交滑移, 形成波纹状花样. 随着变形的不断进行, 波纹状花样平坦化, 最终在断口上形成延伸区.

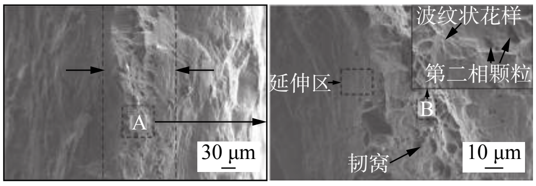

(a) 铜焊丝制备接头断口形貌 (b) 图 8a 中 A 区域高倍图像

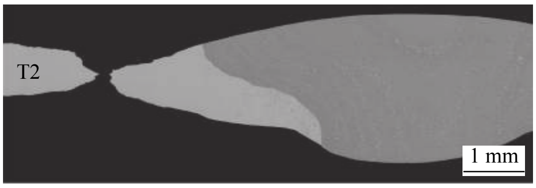

(c) 307Si 焊丝制备接头断裂路径

图 8 断口形貌及断裂路径

Fig. 8 Fracture morphology and fracture path. (a) fracture morphology of the tensile specimen produced by copper filler wire; (b) high-magnification image of zone A Fig. 8a; (c) fracture path of the tensile specimen produced by 307Si filler wire

307Si 焊丝制备接头拉伸试样的断裂路径如图 8c 所示. 断裂同样发生在铜侧热影响区, 因此具有与铜焊丝制备接头相近的抗拉强度.

2.4 腐蚀及电化学试验

铜焊丝制备焊缝的组织为铜基体上分布着富铁球和富铁枝晶. 由图 9 所示焊缝腐蚀形貌可知, 焊缝中富铁相附近的 ε-Cu 基体发生了较为严重的局部电偶腐蚀. 这是因为在 NaCl 溶液中, 富铁相的腐蚀电位高于 ε-Cu 基体[22], 二者之间形成的局部电偶腐蚀加速了 ε-Cu 基体的溶解. 其中, 富铁枝晶成分比较均匀, 在浸泡腐蚀中主要充当阳极, 自身并未发生腐蚀. 而富铁球由于内部存在二次液相分离形成的富铜球以及 σ 相, 自身仍会发生局部腐蚀. 由富铁球的腐蚀形貌可知, 球内的析出相充当阳极, 发生溶解, 在富铁球内留下腐蚀孔洞.

307Si 焊丝制备焊缝的组织为富铁相基体上分布着富铜相和 α-(Fe, Cr) 固溶体. 由图 10 焊缝内的腐蚀形貌可以看出, 焊缝中呈现局部腐蚀特征. 富

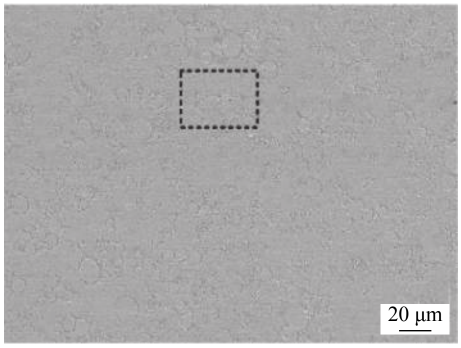

(a) 焊缝

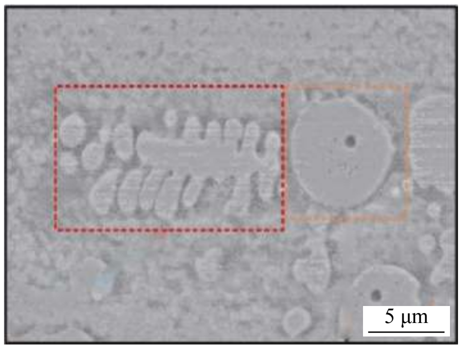

(b) 图 9a 中黑色区域放大

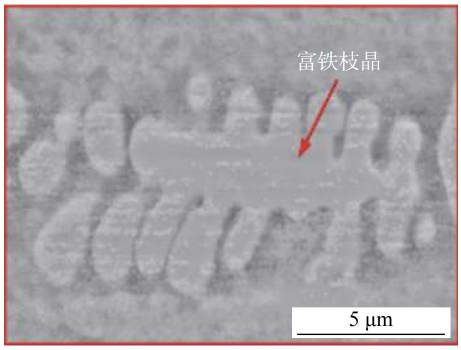

(c) 富铁枝晶

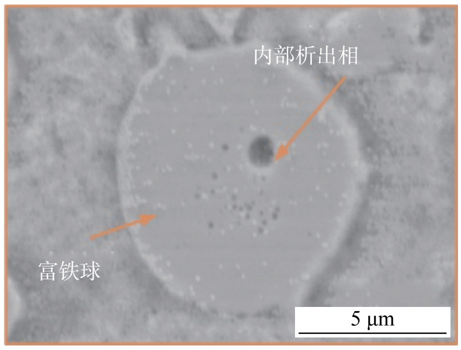

(d) 富铁球

图 9 铜焊丝制备焊缝腐蚀形貌

Fig. 9 Corrosion morphology of weld zone produced by copper filler wire. (a) weld zone; (b) high-magnification image of black box in Fig. 9a; (c) Fe-rich dendrite; (d) Fe-rich spherulites

铁相基体上的富铜相和被铜膜包裹的 α 相脱落, 在基体上形成腐蚀坑. 与铜焊丝制备焊缝类似, 307Si 焊丝制备焊缝中富铁相基体的腐蚀电位高于富铜

相, 半径较小的氯离子穿破钝化膜, 造成富铜相溶解. 而 α-(Fe, Cr) 相被铜膜包裹, 造成 α-(Fe, Cr) 相边界的耐蚀性降低, 铜膜在浸泡腐蚀过程中发生溶解, 导致 α-(Fe, Cr) 相脱落. 熔合线附近的铜母材发生明显的局部腐蚀以及晶间腐蚀, 这是因为界面处和焊缝形成宏观电偶效应增强了熔合线附近的铜基体与富铁相之间的微观电偶腐蚀[23].

使用激光共聚焦显微镜拍摄的铜焊丝及 307Si 焊丝制备焊缝的腐蚀形貌如图 11 所示. 经测算, 铜焊丝制备焊缝中富铁相和周围铜基体的腐蚀深度差为 3.58 μm, 而 307Si 焊丝制备焊缝中富铜相和周围基体的腐蚀深度差为 1.40 μm. 腐蚀深度差越大, 耐蚀程度越高. 铜焊丝制备焊缝中, 铜基体充当

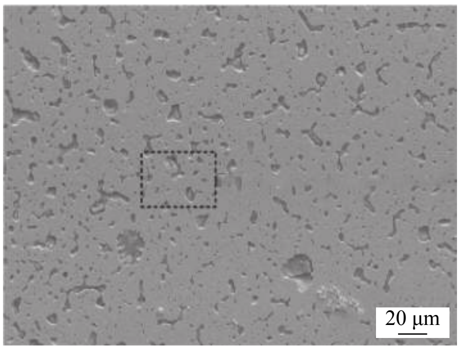

(a) 焊缝

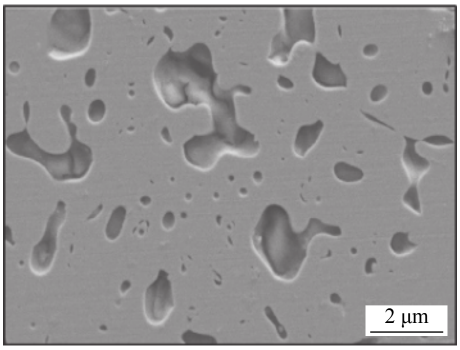

(b) 图 10a 中黑色区域放大

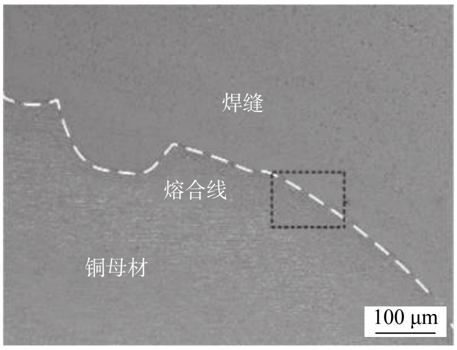

(c) 铜侧界面

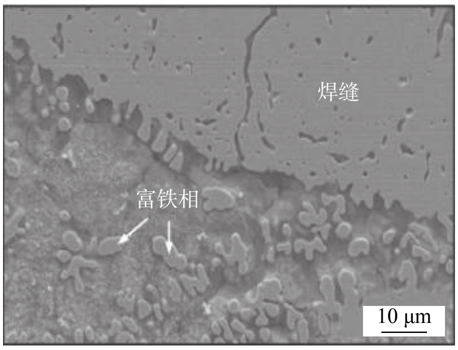

(d) 图 10c 中黑色区域放大

图 10　307Si 焊丝制备接头腐蚀形貌

Fig. 10　Corrosion morphology of joint produced by 307Si filler wire. (a) weld zone; (b) high-magnification image of black box in Fig. 10a; (c) Cu/weld interface; (d) high-magnification image of black box in Fig. 10c

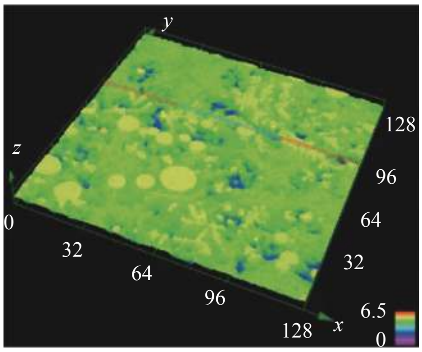

(a) 铜焊丝制备焊缝形貌

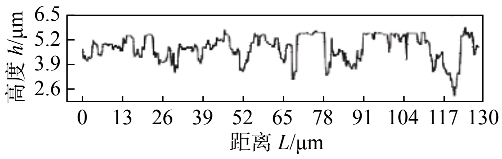

(b) 铜焊丝制备焊缝中腐蚀深度差

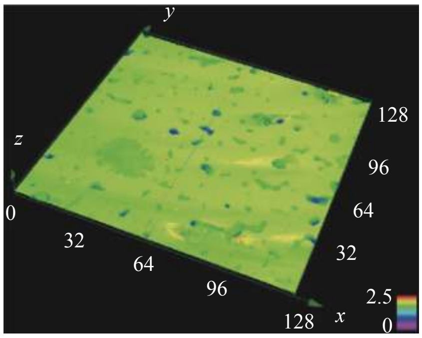

(c) 307Si 焊丝制备焊缝形貌

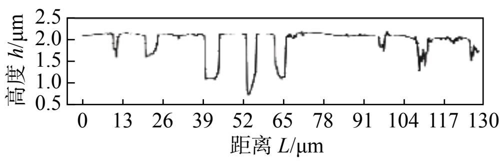

(d) 307Si 焊丝制备焊缝中腐蚀深度差

图 11　浸泡腐蚀试验后焊缝的光学照片

Fig. 11　Optical micrographs of weld after immersion corrosion test achieved by: (a) Cu filler; (b) relative depth of corrosion in weld produced by Cu filler; (c) 307Si filler; (d) relative depth of corrosion in weld produced by 307Si filler

阳极,与 307Si 焊丝制备焊缝相比有着更大的阳极面积和更大的腐蚀深度差,所以耐蚀性低于 307Si 焊丝制备焊缝.

电化学试验结果如图 12、表 5 所示. 腐蚀电位 E_{corr} 反应了金属腐蚀倾向性,腐蚀电位越低说明材料越容易发生腐蚀. 316L 母材因添加了提高耐蚀性的合金元素,有着最高的腐蚀电位;焊缝内由于各物相间构成电偶腐蚀,所以腐蚀电位比成分均一的铜母材低. 母材与两种焊丝制备的焊缝的腐蚀电位高低关系为 $E_{corr316L} > E_{corrT2} > E_{corrCu} > E_{corr307Si}$.

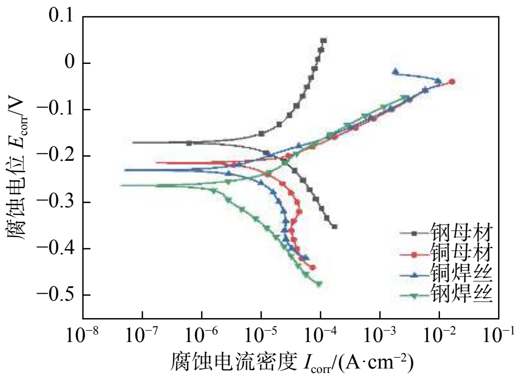

图 12 母材及各焊缝的极化曲线

Fig. 12 Polarization curves of base metals and welds

表 5 母材及焊缝的极化曲线电化学参数

Table 5 Electrochemical parameters simulated from the polarization curves of base metals and welds

材料	腐蚀电位 E_{corr}/V	腐蚀电流 I_{corr}/(10^{-6} A·cm^{-2})
T2	−0.214	14
316L	−0.170	48
纯铜焊丝	−0.229	7.3
307Si焊丝	−0.262	4.8

腐蚀电流密度 I_{corr} 能够反应电极的真实腐蚀速率. 腐蚀电流密度越大,材料的腐蚀程度越高. 虽然铜、钢母材的自腐蚀电流密度最大,但因其在整个接头的浸泡腐蚀过程中主要充当阴极,所以仅发生轻微腐蚀,不应以电化学测量的腐蚀电流密度衡量母材腐蚀程度. 两种焊丝制备焊缝的腐蚀电流密度大小关系为:$I_{corrCu\,焊丝} > I_{corr\,307Si\,焊丝}$,这与激光共聚焦显微镜测量的腐蚀深度差结果相符.

3 结论

(1) 使用纯铜焊丝和 307Si 焊丝均得到了内部无缺陷的铜/钢钨极氩弧焊接头. 拉伸试验中各接头均断裂于铜侧热影响区,铜焊丝制备接头抗拉强度为 219.6 MPa, 307Si 焊丝制备接头抗拉强度为 217.1 MPa, 均超过铜母材强度的 80%.

(2) 两种焊丝制备接头内均发生了铁-铜液相分离,但液相分离程度不同:铜焊丝制备接头中初次液相分离富铁球内部又发生二次液相分离现象,形成了富铜相;307Si 焊丝制备接头中初次液相分离富铜球并未呈现二次液相分离特征.

(3) 在 3.5% NaCl 溶液中,铜焊丝制备接头有着更大的腐蚀深度差和腐蚀电流密度,耐蚀性比 307Si 焊丝制备接头差.

参考文献

[1] Akhtar Awais, Dong Honggang, Xia Yueqing, *et al*. Lap joining 5052 aluminum alloy to Ti6Al4V titanium alloy by GTAW process with AlSi12 filler wire[J]. China Welding, 2020, 29(3): 1 − 8.

[2] 马潇天, 闫德俊, 孟祥晨, 等. 铝/钢搅拌摩擦焊金属间化合物调控研究进展 [J]. 焊接学报, 2020, 41(7): 1 − 11.
Ma Xiaotian, Yan Dejun, Meng Xiangchen, *et al*. Progress on the control of intermetallic compounds in aluminum/steel friction stir welding[J]. Transactions of the China Welding Institution, 2020, 41(7): 1 − 11.

[3] 王志刚. 气化炉 SA387Gr11Cl2 与 316L 异种钢的焊接工艺研究 [J]. 压力容器, 2021, 38(3): 18 − 24.
Wang Zhigang. Study on welding process of SA387Gr11Cl2 and 316L dissimilar steel of gasifier[J]. Pressure Vessel Technology, 2021, 38(3): 18 − 24.

[4] Yingyot P, Samrerng D, Denchay B, *et al*. Gas tungsten arc welding of copper to stainless steel for ultra-high vacuum applications[J]. Journal of Materials Processing Technology, 2020, 277: 116490.

[5] Wang Y, Li X, Wang Xiao, *et al*. Fabrication of a thick copper-stainless steel clad plate for nuclear fusion equipment by explosive welding[J]. Fusion Engineering and Design, 2018, 137: 91 − 96.

[6] Nguyen Q, Azadkhou A, Akbari M, *et al*. Experimental investigation of temperature field and fusion zone microstructure in dissimilar pulsed laser welding of austenitic stainless steel and copper[J]. Journal of Manufacturing Processes, 2020, 56: 206 − 215.

[7] Li J, Cai Y, Yan F, *et al*. Porosity and liquation cracking of dissimilar Nd: YAG laser welding of SUS304 stainless steel to T2 copper[J]. Optics and Laser Technology, 2020, 122: 105881.

[8] Magnabosco I, Ferro P, Bonollo F, *et al*. An investigation of fusion zone microstructures in electron beam welding of copper–stainless steel[J]. Materials Science and Engineering: A,

2006, 424: 163 − 173.

[9] Qi Y, Wang L, Wang S, *et al*. Structural and dynamical heterogeneity of undercooled $Fe_{75}Cu_{25}$ melts with miscibility gap[J]. Journal of Alloys and Compounds, 2014, 615: 962 − 968.

[10] Liu S, Jie J, Guo Z, *et al*. Solidification microstructure evolution and its corresponding mechanism of metastable immiscible $Cu_{80}Fe_{20}$ alloy with different cooling conditions[J]. Journal of Alloys and Compounds, 2018, 742: 99 − 106.

[11] Liu S, Jie J, Dong B, *et al*. Novel insight into evolution mechanism of second liquid-liquid phase separation in metastable immiscible Cu-Fe alloy[J]. Materials and Design, 2018, 156: 71 − 81.

[12] Chen S, Huang J, Xia J, *et al*. Microstructural characteristics of a stainless steel/copper dissimilar joint made by laser welding[J]. Metallurgical and Materials Transactions A, 2013, 44A: 3690 − 3696.

[13] Cheng Z, Huang J, Ye Z, *et al*. Microstructures and mechanical properties of copper-stainless steel buttwelded joints by MIG-TIG double-sided arc welding[J]. Journal of Materials Processing Technology, 2019, 265: 87 − 98.

[14] Meng Y, Li X, Gao M, *et al*. Microstructures and mechanical properties of laser-arc hybrid welded dissimilar pure copper to stainless steel[J]. Optics and Laser Technology, 2019, 111: 140 − 145.

[15] Wang C P, Liu X J, Ohnuma I, *et al*. Thermodynamic database of the phase diagrams in Cu-Fe base ternary systems[J]. Journal of Phase Equilibria and Diffusion, 2004, 25: 320 − 328.

[16] Cao S, Zhao J C. Determination of the Fe-Cr-Mo phase diagram at intermediate temperatures using dual-anneal diffusion multiples[J]. Journal of Phase Equilibria and Diffusion, 2016, 37: 25 − 38.

[17] Gao X L, Li L K, Liu J, *et al*. Effect of laser offset on microstructure and mechanical properties of laser welding of pure molybdenum to stainless steel[J]. International Journal of Refractory Metals & Hard Materials, 2020, 88: 105186.

[18] Yang Y, Busby J T. Thermodynamic modeling and kinetics simulation of precipitate phases in AISI 316 stainless steels[J]. Journal of Nuclear Materials, 2014, 448: 282 − 293.

[19] Wu Y H, Wang W L, Chang J, *et al*. Evolution kinetics of microgravity facilitated spherical macrosegregation within immiscible alloys[J]. Journal of Alloys and Compounds, 2018, 763: 808 − 814.

[20] Alvaro M, Stefan K, Diego N, *et al*. Solutal Marangoni flow as the cause of ring stains from drying salty colloidal drops[J]. Physical Review Fluids, 2019, 4: 041601.

[21] Ebara R, Takeda K, Ishibashi Y, *et al*. Microfractography in failure analysis of cold forging dies[J]. Engineering Failure Analysis, 2009, 16: 1968 − 1976.

[22] San X Y, Zhang B, Wua B, *et al*. Investigating the effect of Cu-rich phase on the corrosion behavior of Super 304H austenitic stainless steel by TEM[J]. Corrosion Science, 2018, 130: 143 − 152.

[23] Chen Y, Wang Y, Zhou L, *et al*. Macro-galvanic effect and its influence on corrosion behaviors of friction stir welding joint of 7050-T76 Al alloy[J]. Corrosion Science, 2020, 164: 108360.

第一作者: 朱元皓，硕士；主要研究方向为异种金属焊接；Email: dutzhuyh@163.com.

通信作者: 董红刚，博士，教授；Email: donghg@dlut.edu.cn.

（编辑：　胡广旭）

MAIN TOPICS, ABSTRACTS & KEY WORDS

Influence of Zn evaporation on wetting of Ag-Cu-Zn brazing alloy on TiC-Ni cermet LI Yulong[1,2], WU Haoyue[1], LEI Min[1] (1. Key Lab for Robot and Welding Automation of Jiangxi Province, Nanchang University, Nanchang, 330031, China; 2. Center for Advanced Lifecycle Engineering, University of Maryland, Maryland, 20742, USA). pp 1-6

Abstract: Wetting of Ag-Cu-Zn brazing alloy on TiC-Ni cermet was performed. The results show that continuous (Cu, Ni) layer forms at the interface of Ag-Cu-Zn/TiC-Ni cermet at 810 ℃ for 10 min with a heating rate of 22.5 ℃/min in vacuum. The whole wetting process contains an incubation stage, a spreading stage, a pinning stage, a receding stage, and an equilibrium stage. The equilibrium contact angel is 27.3°. With the increase of heating rate from 10 ℃/min to 30 ℃/min, the evaporation velocity of Zn strengthens; the lasting time of the spreading process shortens, and the amount of (Cu, Ni) at the interface decreases. As a result, the equilibrium contact angel of Ag-Cu-Zn on TiC-Ni cermet increases with the heating rate. The evaporation of Zn weakens in argon. Only a little (Cu, Ni) forms at the interface of Ag-Cu-Zn/TiC-Ni cermet in argon, although the Ag-Cu-Zn brazing alloy dissolves a great amount of Ni matrix. So the base diameter firstly increases and the contact angle decreases with time, then the base diameter almost remains unchanged, and the contact angle increases slightly.

Highlights: The effect of Zn evaporation on the wettability of Ag-Cu-Zn brazing alloy on TiC-Ni surface was studied at different rates in vacuum and argon atmosphere, respectively.

Key words: Ag-Cu-Zn; wetting; TiC-Ni cermet; interface; evaporation

Effect of ultrasonic peening on fatigue performance of aluminum alloy FSW joints with root defects ZHAN Rui[1], WANG Dongpo[1,2], DENG Caiyan[1,2], CUI Lei[1,2], GUAN Wei[1], LIANG Hang[1] (1. Tianjin University, Tianjin, 300072, China; 2. Tianjin Key Laboratory of Advanced Joining Technology, Tianjin, 300072, China). pp 7-12

Abstract: Four-point bending fatigue tests were carried out to investigate the effects of ultrasonic impact treatment (UIT), ultrasonic peening (UP) and UIT + UP on the fatigue properties of aluminum alloy FSW joints with root "kissing bonding" defects, and the mechanism of the fatigue performance improvement was explored by analyzing the defect morphologies, microhardness values and residual stress distributions of the samples before and after treatments. Compared with the result that the fatigue strength of FSW joints treated by ultrasonic impact treatment at the root is improved only under 2×10^6 cycles, the results show that UP and UIT + UP can significantly improve the high-cycle fatigue performance, and the fatigue strength is increased by 13% and 40% respectively, corresponding to 2×10^6 cycles. UIT combined with UP cannot only form the compact work hardening layer at the root defects of the FSW joint, increase the microhardness, but also introduce the wider compressive residual stress region near the weld root by UP, eliminate the fold defects probably caused by UIT, significantly improving the fatigue performance.

Highlights: (1) Improvements of the fatigue life of FSW joints with the root "kissing bonding" defects were accomplished by ultrasonic impact techniques.
(2) Mechanisms on the enhancement of the fatigue life of FSW joints with the root "kissing bonding" defects were explained.

Key words: ultrasonic impact treatment; FSW; root kissing bonding defect; fatigue performance; residual stress

Effect of filler metals on microstructure and properties of T2 copper/316L stainless steel GTAW joint ZHU Yuanhao, WU Baosheng, GUO Baizheng, LI Peng, DONG Honggang (Dalian University of Technology, Dalian, 116024, China). pp 13-21

Abstract: T2 copper/316L stainless steel dissimilar joints were produced by gas tungsten arc welding with Cu filler wire and 307Si filler wire, respectively. The effect of filler metals on microstructure, mechanical properties and corrosion resistance of the joints was investigated. The microstructure of copper/steel weld was largely affected by liquid phase separation between iron and copper. When Cu filler wire was used, Fe-rich spherulites formed by Fe-Cu primary liquid phase separation distributed in the weld. Inside the Fe-rich spherulites, minority Cu-rich spheres formed by secondary liquid phase separation. However, when 307Si filler wire was used, the primary liquid phase separated Cu-rich spherulites showed no characteristic of secondary liquid phase separation. The tensile specimens achieved by both filler wires fractured at HAZ on the copper side, and the strength of each joints reached at least 80% of Cu base metal. Dimples and stretched zone were distributed on the fracture, showing the ductile fracture mode. Compared to the joint achieved by 307Si filler wire, the joint achieved by Cu filler had larger corrosion depth and corrosion current density, showing an inferior corrosion resistance.

Highlights: (1) Defect-free copper/steel GTAW joints were produced by Cu filler wire and 307Si filler wire, respectively.
(2) The microstructure formation mechanism of copper/steel joint was analyzed based on the Fe-Cu liquid phase separation theory.
(3) The effect of microstructure inhomogeneity on corrosion resistance of joints achieved by Cu filler wire and 307Si filler wire was analyzed.

Key words: copper/steel dissimilar joint; gas tungsten arc welding; microstructure; mechanical property; corrosion resistance

Explosive welding and performance test of $Al_{0.1}CoCrFeNi$ high-entropy alloy/TA2 composite plate TIAN Qichao[1], MA Honghao[1,2], SHEN Zhaowu[1], CHEN Zijun[1], ZHAO Kai[1], Zhao Yang[3] (1. Key Laboratory of Material Mechanics Behavior and Design, Chinese Academy of Sciences, University of Science and Technology of China, Hefei, 230027, China; 2. State Key Laboratory of Fire Science, University of Science and Technology of China, Hefei, 230027, China; 3. National Key Laboratory for Remanufacturing, Army Academy of Armored Forces, Beijing, 100072, China). pp 22-29

Abstract: High-entropy alloy (HEA) is an emerging material which possesses great potential as a structure material, but there are relatively few studies devoted to HEA joining technology. The TA2 commercial pure titanium plate and $Al_{0.1}CoCrFeNi$ HEA are joined by explosive welding technology. The microstructure analysis and mechanical tests of $Al_{0.1}CoCrFeNi$/TA2 composite plate are conducted. These results show that the $Al_{0.1}CoCrFeNi$/TA2 composite plate possesses a wavy bonding interface with a discontinuous melted zone. Moreover, the melted zone presents a multi-element mixed state, and a relatively uniform element distribution occurs in the melted zone. The hardness of the melting zone is greater than that of TA2 side and $Al_{0.1}CoCrFeNi$ HEA side. And it gradually decreases with the increase of the distance from the interface. However, the hardness of the composite plate is still higher than that of the parent materials. Compared with the strength of the $Al_{0.1}CoCrFeNi$ HEA plate (398 MPa), the strength of the $Al_{0.1}CoCrFeNi$/TA2 composite plate after explosive welding is significantly increased (567 MPa). On the contrary, elongation is reduced after explosive welding. The results tests show that explosive welding is an effective method for joining TA2 commercial pure titanium with $Al_{0.1}CoCrFeNi$ high-entropy alloy, and the welded composite plate shows great mechanical performance.

Highlights: (1) The composite plate between high entropy alloy and titanium was fabricated by explosive welding.
(2) Through the process control of explosive welding process, a large number of compounds at the interface are avoided.

Key words: explosive welding; high-entropy alloy; titanium alloy; microstructure; mechanical properties

Research status and development trend of titanium/steel bimetallic composite plates of welding HU Fengya[1,2], XU Guojing[1], CHEN Wei[1], LENG Xuesong[1], FU Kuijun[2], YAN Jiuchun[1] (1. State Key Laboratory of Advanced Welding and Joining, Harbin Institute of Technology, Harbin, 150001,